frontiers | Frontiers in Chemical Engineering

TYPE Original Research
PUBLISHED 29 July 2024
DOI 10.3389/fceng.2024.1352283

OPEN ACCESS

EDITED BY
Ranjith G. Nair,
National Institute of Technology, India

REVIEWED BY
Shirley Selahle,
University of Venda, South Africa
Lethula Mofokeng,
University of Pretoria, South Africa

*CORRESPONDENCE
Andile Mkhohlakali,
Andilem@mintek.co.za

RECEIVED 07 December 2023
ACCEPTED 13 June 2024
PUBLISHED 29 July 2024

CITATION
Mkhohlakali A, Jen T-C, Ledwaba K, Mapukata S, Mabowa HM, Letsoalo MR, Ntsasa N and Tshilongo J (2024), Influence of surfactant on sol-gel-prepared TiO_2: characterization and photocatalytic dye degradation in water. *Front. Chem. Eng.* 6:1352283. doi: 10.3389/fceng.2024.1352283

Influence of surfactant on sol-gel-prepared TiO_2: characterization and photocatalytic dye degradation in water

Andile Mkhohlakali[1]*, Tien-Chien Jen[2], Kabelo Ledwaba[2,3], Sivuyisiwe Mapukata[4], Happy Mothepane Mabowa[1,5], Mokgehle R. Letsoalo[1], Napo Ntsasa[1] and James Tshilongo[1,5]

[1]Analytical Chemistry Division, Mintek, Randburg, South Africa, [2]Department of Mechanical Engineering Science, University of Johannesburg, Johannesburg, South Africa, [3]Department of Chemical Engineering University of South Africa, Johannesburg, South Africa, [4]Nanotechnology Innovation Centre (NIC), Advanced Materials Division, Mintek, Randburg, South Africa, [5]School of Chemistry, University of the Witwatersrand, Johannesburg, South Africa

In this study, Titanium dioxide (TiO_2) nano-powder was prepared using a sol-gel process with and without surfactant. A typical non-ionic surfactant (Triton X-100) was used during the process. The phase compositions of TiO_2 and surfactant-assisted TiO_2 (TiO_2-sa) were investigated by FTIR, X-ray diffraction (XRD), scanning electron microscope-energy dispersive spectroscopy (SEM-EDS), and thermogravimetric analysis (TGA). Brunauer–Emmett–Teller (BET) was used to determine the nano-powder's specific surface area and pore size distribution. Moreover, transmission electron microscopy (TEM) and selected area electron diffraction (SAED) analysis exhibited particle size in the range of 65–85 nm and polycrystalline phase, respectively. UV-vis spectrophotometer showed high absorption as dominating the visible region (438–450 nm) with relative redshift and reduced bandgap from 2.98 to 3.12 eV upon adding surfactant on TiO_2. X-ray fluorescence spectroscopy (XRF) exhibits high purity TiO_2 with more than 82% composition with the lowest relative standard deviation (RSD %). Moreover, the photoluminescence (PL) of TiO_2-sa showed enhanced oxygen vacancies and surface defects which reduce the direct electron-photon (e/h+) pair recombination. TiO_2-sa illustrated promising characteristic features of an active photocatalyst for the degradation of organic pollutants.

KEYWORDS

sol-gel, surfactant assisted, TiO_2 nano-powder, optical properties, MB degradation

1 Introduction

Water contamination caused by textile dyes and other industrial dyestuffs has become a worldwide concern (Lellis et al., 2019; Liang et al., 2018). The most commonly used dyes are classified as organic contaminants, with colored waste released into the water streams during dying process—a primary source of environmental damage (Shindhal et al., 2021). Furthermore, toxic byproducts generated in wastewater as a result of oxidation, hydrolysis, or other chemical reactions are considered hazardous to human health (Dougna et al., 2015). Over the past decade, TiO_2 has shown potential for the removal of

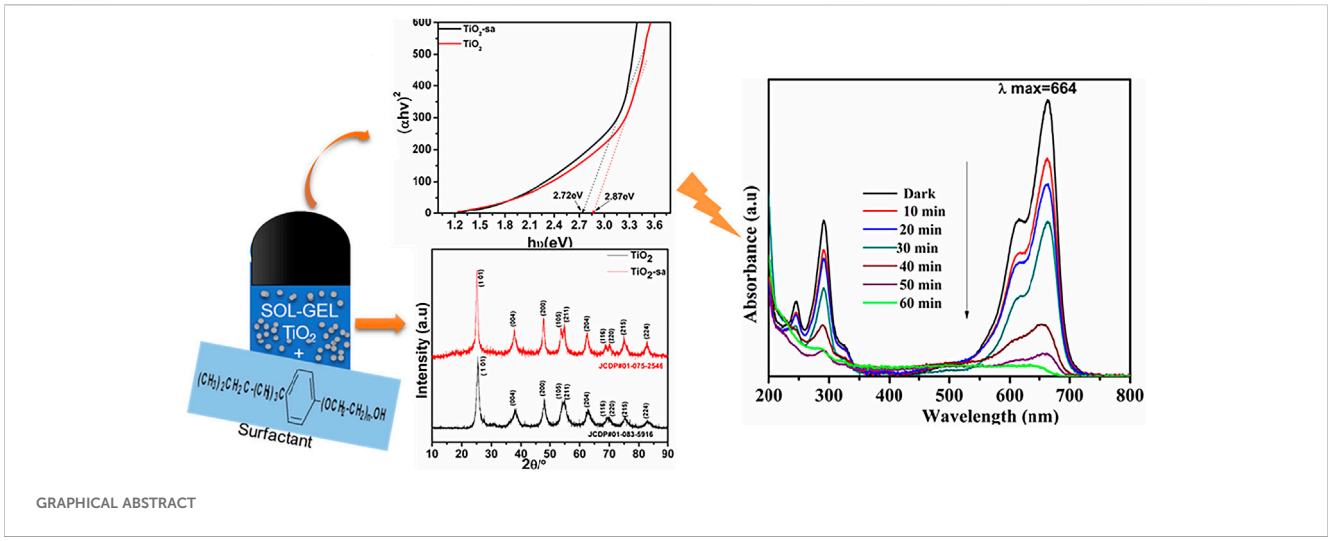

GRAPHICAL ABSTRACT

organic pollutants such as methylene blue (MB), methyl orange (MO), and phenols under UV light and little visible light and air to produce hydroxyl that destroys organic dyes in photocatalytic process (Basavarajappa et al., 2020). However, the lack of visible region absorption, among other issues, is a bottleneck in this process. TiO_2 nanostructures have attracted great attention in numerous applications including ceramics, photocatalysts, photovoltaic cells, photoanodes, and sensors (Wang et al., 2009; Bahar et al., 2017).

TiO_2 is known to exist in nature in three various crystalline phases; brookite, anatase, and rutile (Allen et al., 2018; Hanaor and Sorrell, 2011). Unlike the other crystalline phases, the anatase form has a greater surface area, is more stable, and has higher activity (Ola and Maroto-Valer, 2015). The chemical, physical, and photocatalytic properties of TiO_2 are greatly influenced by the phase of the structure, and morphology is a crucial factor in assessing the material's appropriateness for discrete applications (Andronic et al., 2011). TiO_2 generally has a broad bandgap equivalent to 3.2 eV along with a high surface area and is relatively non-toxic; however, it only absorbs 5% of solar radiation (energy), with the remainder being UV-Vis (Casino et al., 2014; Anderson and Bard, 1995). Furthermore, TiO_2 has a high rate of charge recombination of photogenerated electrons and holes. Scientists have used several techniques, including doping, to address the limitations of TiO_2 so as to make it a more efficient photocatalyst (Anderson and Bard, 1995).

The chemical and physical properties of metal oxide nanomaterials can be controlled by the process used to prepare them, which in turn influences the photocatalytic activity (Zhou, 2020). TiO_2 nanomaterials have been successfully synthesized utilizing a variety of methods, including hydrothermal synthesis, micro-emulsion, physical vapor deposition (PVD), chemical vapor deposition (CVD), and sol-gel (Zhou, 2020; Karami, 2010; Dubey, 2018; You et al., 2014). The Stöber sol-gel procedure, which was developed for the nuclear sector in 1960s, is one of the most commonly used methods for preparing metal oxides due to its ease of preparation, high degree of homogeneity, low cost (Dubey, 2018; Mohamad Saad et al., 2015), and the possibility of forming small particles at room temperature (Bahar et al., 2017; Id, 2018; Zhai et al., 1990; Attia et al., 2002). It involves controlling the NPs' surface chemistry, size, shape, and photo-stability to further enhance photocatalytic efficiency. The studies referenced reported the hydrolysis of tetraethyl orthosilicate (TEOS), Si (OC_2H_5), under acid condition to form SiO_2-based glass (Zhai et al., 1990; Alothman et al., 1990). However, this approach results in nanoparticle aggregation, which lowers the effective surface area of metal oxides.

The surfactant is one of the key factors that influence the structure-composition and photocatalytic characteristics of TiO_2. Surfactants are used in this process to reduce and improve agglomeration. Surface directing agent (SDA) acts as a template and decreases surface tension while enhancing crystal nucleation and development in the reaction (Huang et al., 2014). It also serves as an effective medium for reducing the internal radius of particles, which in turn reduces their size and effectively addresses the aggregation issue (Feinle et al., 2015). In addition, surfactant and acid are used to trigger repulsive force between the particles as a result of proton adsorption that positively charges uncharged precipitates (Galkina et al., 2011).

Feinle et al. (2015) investigated the effects of surfactant and acid on sol-gel-produced MgO aerogels, resulting in surfactant to aid particle dispersion. Andrade-Guela et al. (2018) reported the phase formation of TiO_2 upon the application of hydrochloric and acetic acids as (hydrolysis agents) catalysts. Few studies are evident that narrow down to the effect of surfactant on TiO_2-photocatalyst for fine-tuning morphological, optical, and photocatalytic properties.

This study investigates the structure-morphology and photocatalytic MB dye degradation performance of TiO_2 upon the addition non-ionic surfactant (Triton X100) prepared by a sol-gel process. The optical properties, morphology, and phase compositions were characterized using ultraviolet–visible (UV-Vis), photoluminescence (PL) spectroscopy, X-ray diffraction (XRD), scanning electron microscopy-energy dispersive spectroscopy (SEM-EDS), high-resolution transmission electron microscopy (TEM), Brunauer–Emmett–Teller (BET), Fourier transform infrared (FTIR), thermogravimetric analysis (TGA), and X-ray fluorescence spectroscopy (XRF) methods.

2 Experimental section

2.1 Synthesis and characterization

The Stöber sol-gel method was used to prepare surfactant-assisted and -free TiO_2 nanoparticles. Titanium (IV)

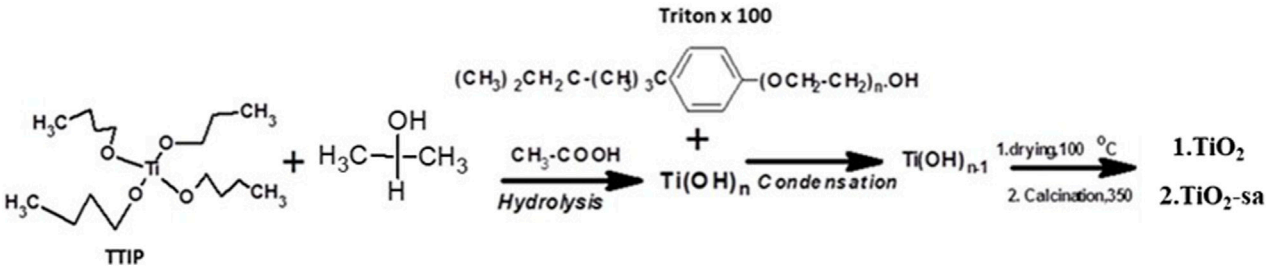

FIGURE 1
Synthetic route of sol-gel process for TiO_2 and TiO_2-sa.

isopropoxide $Ti(O_iPr)_4$ (70%, Merck), isopropanol (97%, Sigma Aldrich), and Triton X-100 (Merck) were used as precursor, solvent, and surfactant, respectively. To prepare TiO_2 and surfactant assisted-TiO_2 (TiO_2-sa), an acid hydrolysis agent was used that was composed of a mixture of 2 M acetic acid in isopropanol (1:1 v/v). In a 100 mL beaker, 2 mL of $Ti(OiPr)_4$ was added to 20 mL of isopropanol and stirred vigorously for 30 min at 25 °C. Then, a solution containing 2 mL ethanol and 1 mL acetic acid was added while stirring, and the dense solution was stirred for 1 h until a white gel was formed. With regard to TiO_2-sa, 2 mL Triton X-100 was added to the mixture of $Ti(OiPr)_4$ and isopropanol, and the solution was continually stirred for 1 h to form a dense gel-like solution. This with precipitate was dried in an oven at 80 °C–100 °C for 1 h to form a mixture of dried gel and powder. A mortar and pestle were then used to grind to obtain white powder. Finally, the powder was calcined in a furnace at 350 °C for 1 h. The process for the afromentioned method is illustred in Figure 1

2.2 Photocatalytic degradation of methylene blue dye

The photocatalytic activity of as-prepared TiO_2 and TiO_2-sa photocatalysts were evaluated by monitoring the photodegradation of MB (at λmax = 664 nm) maximum absorption band in aqueous solution (600 mL) of 20 ppm, 0.0129 mg of MB, and 0.15 g of the requisite amount of TiO_2-based photocatalyst mixed in a beaker. Before the irradiation employing light source (150 W Xenon filament lamp) and 627 nm wavelength under ambient conditions, the TiO_2 + MB was stirred by magnetic stirrer in the dark for 30 min to maintain conformal dispersion of the photocatalyst with reduced aggregation. Then 20 mL was filtered using micro filters and taken for UV-vis analysis. The TiO_2 + MB sample was stirred under irradiation with the light source situated horizontal above the beaker. At different time intervals (10, 20, 30, 40, 50 min, 1 h), 5 mL of aqueous solution was taken was taken for UV-vis spectrophotometer analysis on UV 180 (Thermofisher).

2.3 Characterization of TiO_2 based materials

The FTIR (Bruker vertex 70) technique was used to analyze the bond stretching frequencies of TiO_2. The structure and crystallinity phase of TiO_2-based materials were determined using powder XRD, Bruker D8 advanced diffractometer, 20 kV and 40 mA operation, Cu-K radiation, = (1.54060°A). The patterns were obtained at 10–90° at a scan rate of 2°min−1. Field emission scanning electron microscopy (FE-SEM) was performed using JEOL JSM-7800F with an EDS detector for elemental composition. Selected area electron diffraction (SAED) with the HRTEM analyses were performed on a JEOL (JEM-2010, Japan) at an accelerating voltage of 200 kV. ImageJ was used to obtain particle size. Thermal analysis was conducted using TGA SDTQ-600 (Advanced Laboratory Solutions) at a heating rate of 10 °C/60 s with nitrogen gas (N_2) flow. N_2 adsorption–desorption was determined at 77 K. The specific surface area (SBET) of the monolayer coverage was determined using the BET method. Pore size distribution was measured from the adsorption branch of isotherm by the Barrett–Joyner–Halenda (BJH) method. UV-vis absorption spectra of the materials were obtained on UV 180 (Thermofisher). XRF was used to determine the elemental composition using an XRF gun X-MET8000 (expert Geo) from Hitachi.

3 Results and discussion

In Figure 2, all XRD patterns exhibit highly crystalline structures indexed at (101), (004) (200), (105), (211), (204), (116), (220), (215), and (224), corresponding to 2θ = 25.2°, 37.5°, 47.8°, 54.2°, 55°, 62.7°, 68.09°, 70.2°, 75°, and 82°, respectively. These results were assigned to tetragonal TiO_2 anatase and matched JCPD standards 01-083-5916 and 01-075-2546 for TiO_2 and TiO_2-sa, respectively. The XRD pattern showed no additional peaks, indicating that the as-synthesized TiO_2-based has no impurities. Both TiO_2 structures preferred anatase orientation, which might be due to the application of a weak acid such as acetic acid at room temperature and low calcination temperature (350 °C) which aligned with Wong et al. (2014). It is worth noting that only anatase TiO_2 was identified here, with no rutile phase; this could be attributed to the low concentration of oxygen vacancies caused by high oxygen concentration during particle growth, preventing changeover from anatase to rutile phases (Zhao et al., 2007). The crystallite size of the as-prepared TiO_2 nano-powders was calculated from XRD patterns. Using the Debye–Scherrer formula, the average crystallite size of the TiO_2 nano-powder produced was determined (Wu et al., 2008; Thiruvengadathan et al., 2013; Wang et al., 2015) Eq. 1:

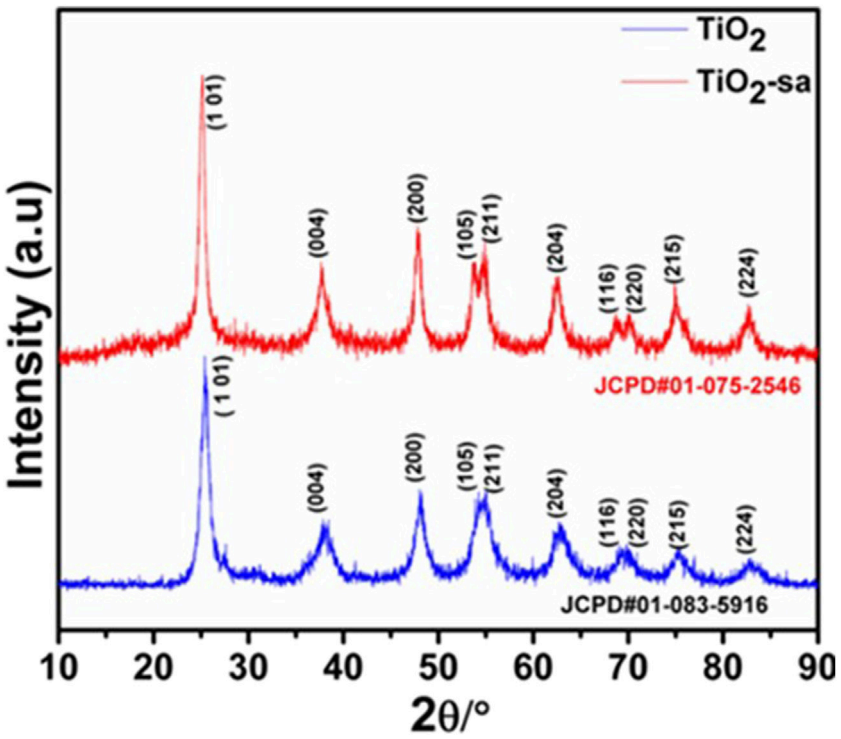

FIGURE 2
XRD patterns for TiO_2 and TiO_2-sa.

TABLE 1 Average crystalline size and phase of TiO_2 nano-powders.

Materials	Av. crystalline size(nm)	Crystalline phase (%)	Crystal structure
TiO_2	38.26	Anatase 100	Tetragonal
TiO_2-sa	40.01	Anatase 100	Tetragonal

$$D = 0.9\lambda/\beta\cos\theta \quad (1)$$

The crystallite diameter is represented by D, the wavelength of Cu by λ, the Bragg's angle is θ, the full width at half maximum (FWHM) of the greatest intense diffraction planes is represented by β, Scherer's constant is 0.9, and the correction factor allows for particle shape (Mahshid et al., 2007). The average crystalline sizes were calculated as 38.26 and 40.01 nm; XRD data are presented in Table 1.

TGA/DTA (Figures 3A, B) was employed to evaluate the composition/decomposition and thermal stability of the as-prepared TiO_2 nano-powders. The rapid decay observed around 90 °C–180 °C was ascribed to the decomposition of the adsorbed water molecules, followed by the loss of solvent (isopropyl alcohol) (Fang et al., 2015; Alothman, 2016; Phattepur et al., 2019). The results aligned with Fang et al. (2015) and Kubiak et al. (2020). It was observed that TiO_2-sa had the highest weight loss (%), which was also attributed to the decay of Triton X-100. After 350 °C, thermograph curves displayed a plateau, perhaps due to the complete loss of solvent and Triton X-100; at this region, TiO_2 is thermal stable (Phattepur et al., 2019). Notably, TiO_2-sa showed late decomposition, which indicated that it resisted heat better than TiO_2 nano-powder. The further decay of TiO_2-sa after 850 °C might correspond to the beginning of the transformation of anatase to rutile, as described in Li J. et al. (2020) and Wetchakun and Phanichphant (2008). In addition, Figure 3B indicates the derivative of the TGA, which represents the temperature values at specific weight loss. For instance, the first 17.02% loss happened at 45 °C, followed by 8.35% at 240 °C for TiO_2. In contrast to TiO_2-sa, the highest weight loss of 48.78% occurred at 330 °C.

Figures 4A and B represent BET results for N_2 adsorption/desorption isotherms at 77K, BET specific surface area, pore volume and BJH pore size distribution of TiO_2 and TiO_2-sa. It was observed that the isotherms of as-synthesized TiO_2 nano-powders demonstrated a typical type-II isotherm as the International Union of Pure and Applied Chemistry (IUPAC) defines the H3 type. It is noteworthy that a hysteresis loop can be seen in the p/p^o ranges of 0.6–1.0 and 0.75–1.0 for TiO_2 and TiO_2-sa isotherms, respectively. The obtained results suggested the existence of interconnected mesoporous TiO_2 nano-powders, similar to that reported in literature [34]. Furthermore, upon the addition of Triton X-100, loop hysteresis shifted to high relative pressures (p/p^o), indicating pore volume transformation. Kubiak et al. (2020) compared BET and BJH parameters for Triton X-100-assisted TiO_2 and pluronic P123-assisted TiO_2 and found that pore volume and specific surface area were enhanced and the hysteresis loop shifted to higher pressure regions for assisted TiO_2. BET-specific surface area, average pore size, and pore volume are summarized in Table 2. The incorporation of a

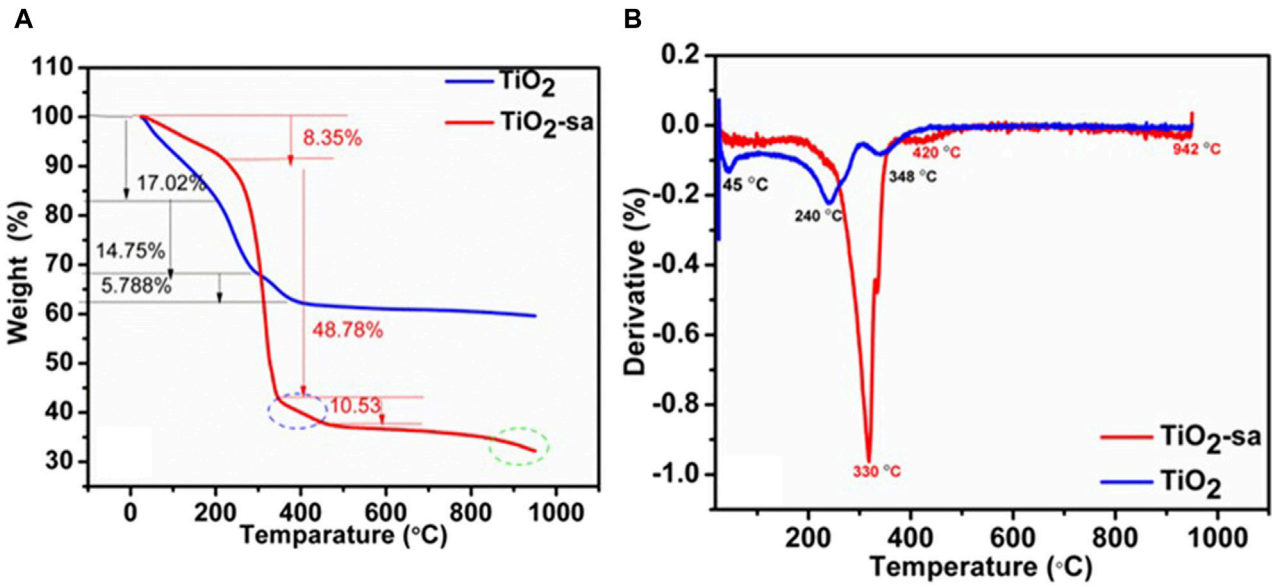

FIGURE 3
(A) TGA and **(B)** DTA data for TiO2 and TiO2-sa.

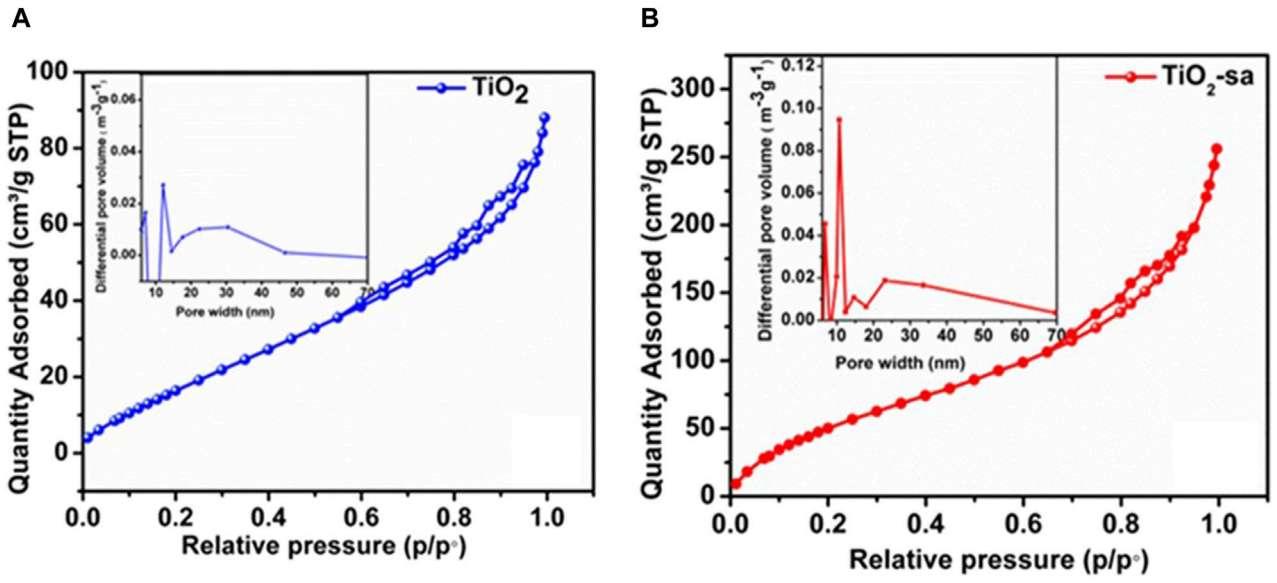

FIGURE 4
N_2 adsorption/desorption isotherm and corresponding BJH pore size distribution: insert of **(A)** TiO_2 and **(B)** TiO_2-sa.

TABLE 2 BET results of TiO_2 and TiO_2-sa nano-powders.

Materials	BET (m^2/g)	Average pore size (nm)	Pore volume (m^3/g)
TiO_2	90.00	0.13	0.20
TiO_2-sa	150.00	0.58	0.37

Triton X-100 contributed to the increase of specific surface area—150 cm^2 g^{-1} in contrast to its counterpart at 90 cm^2 g^{-1}. In addition, pore size distribution (Figures 5A, B: insert) was correlated to the above results, where two prominent peaks centered at around 10–30 nm. The average pore size was 0.13 nm for TiO_2 and 0.58 nm for TiO_2-sa. Nonetheless, mesoporous volume increased from 0.20 cm^3 g^{-1} for TiO_2 to 0.37 cm^3 g^{-1} for TiO-sa. Surfactant was able to modify pore size, pore volume, and specific surface area.

Figures 5A–F display the SEM-EDS images of TiO^2 and TiO_2-sa. TiO_2 showed well-defined nanoparticle surface morphology. Aggregated spheres could be caused by the nature of the sol-gel process. EDS revealed the existence of Ti and O, which confirmed

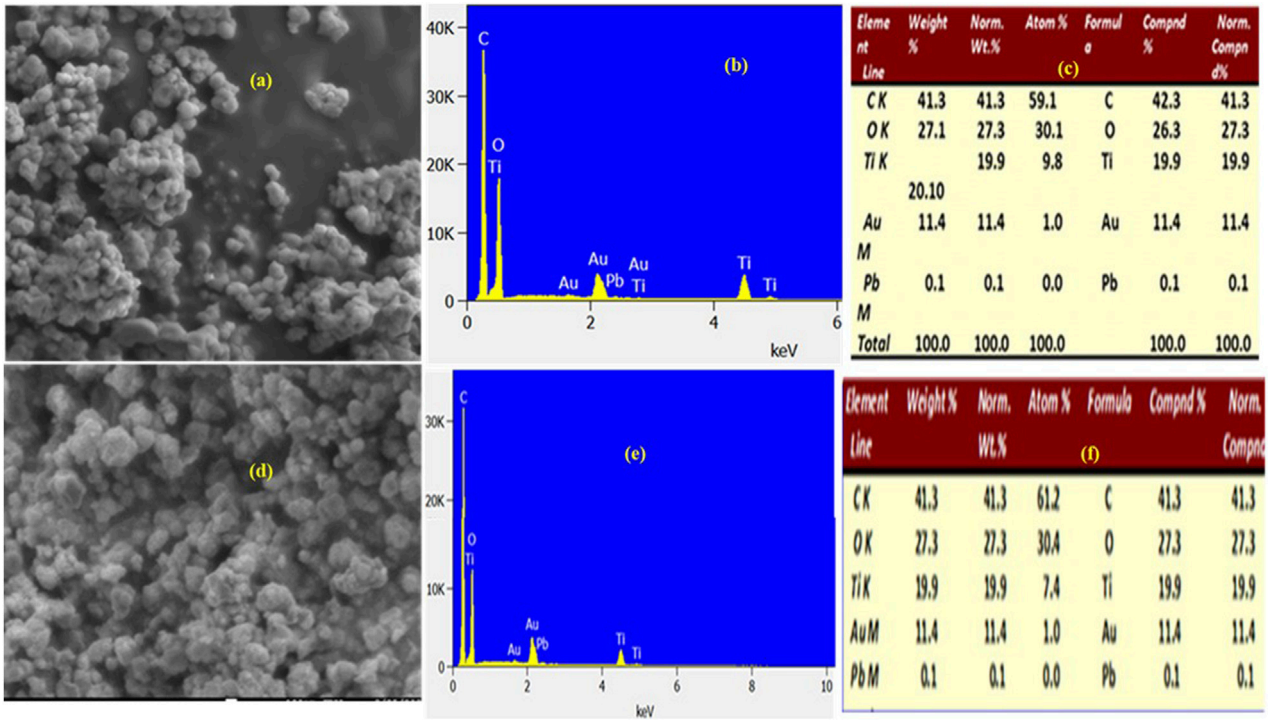

Element Line	Weight %	Norm. Wt.%	Atom %	Formula	Compnd %	Norm. Compnd%
C K	41.3	41.3	59.1	C	42.3	41.3
O K	27.1	27.3	30.1	O	26.3	27.3
Ti K	20.10	19.9	9.8	Ti	19.9	19.9
Au M	11.4	11.4	1.0	Au	11.4	11.4
Pb M	0.1	0.1	0.0	Pb	0.1	0.1
Total	100.0	100.0	100.0		100.0	100.0

Element Line	Weight %	Norm. Wt.%	Atom %	Formula	Compnd %	Norm. Compnd
C K	41.3	41.3	61.2	C	41.3	41.3
O K	27.3	27.3	30.4	O	27.3	27.3
Ti K	19.9	19.9	7.4	Ti	19.9	19.9
Au M	11.4	11.4	1.0	Au	11.4	11.4
Pb M	0.1	0.1	0.0	Pb	0.1	0.1

FIGURE 5
FE-SEM and EDS data for **(A–C)** TiO_2 and **(C–F)** TiO_2-sa.

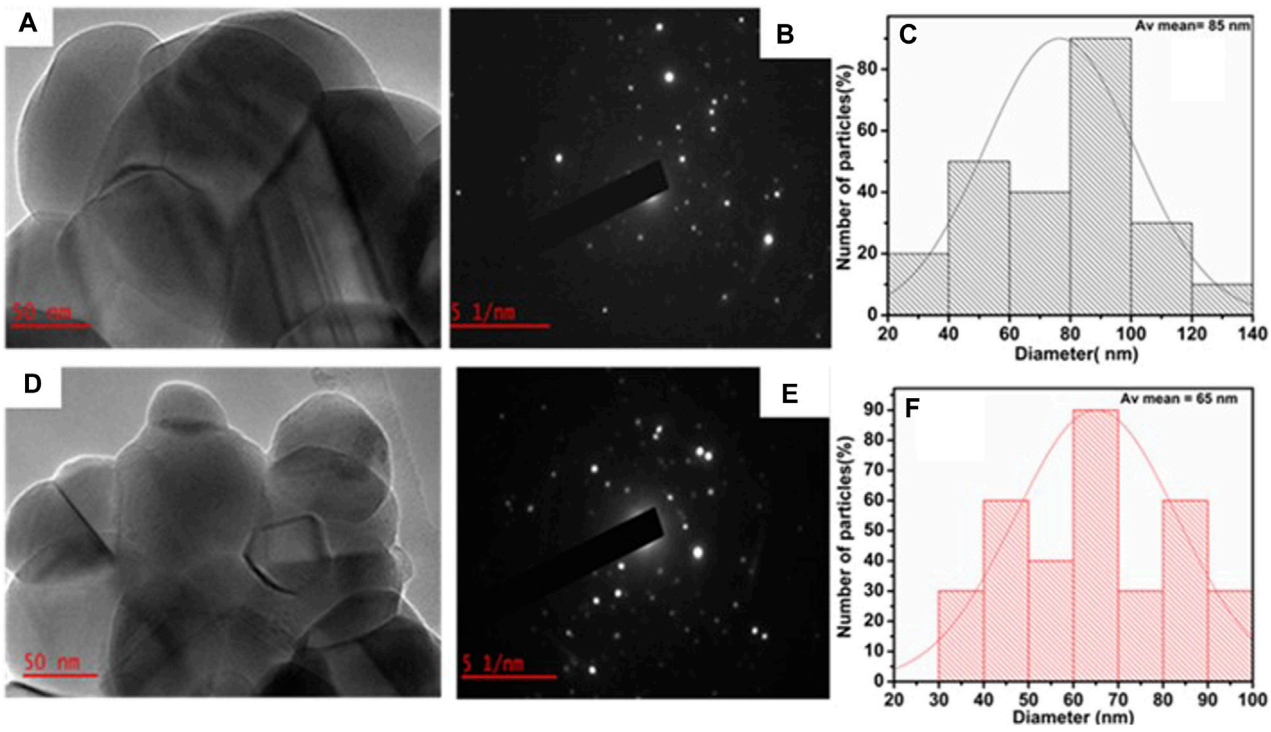

FIGURE 6
HR-TEM, SAED micrograph data, and histogram of **(A–C)** TiO_2 and **(D–F)** TiO_2-sa.

10.3389/fceng.2024.1352283

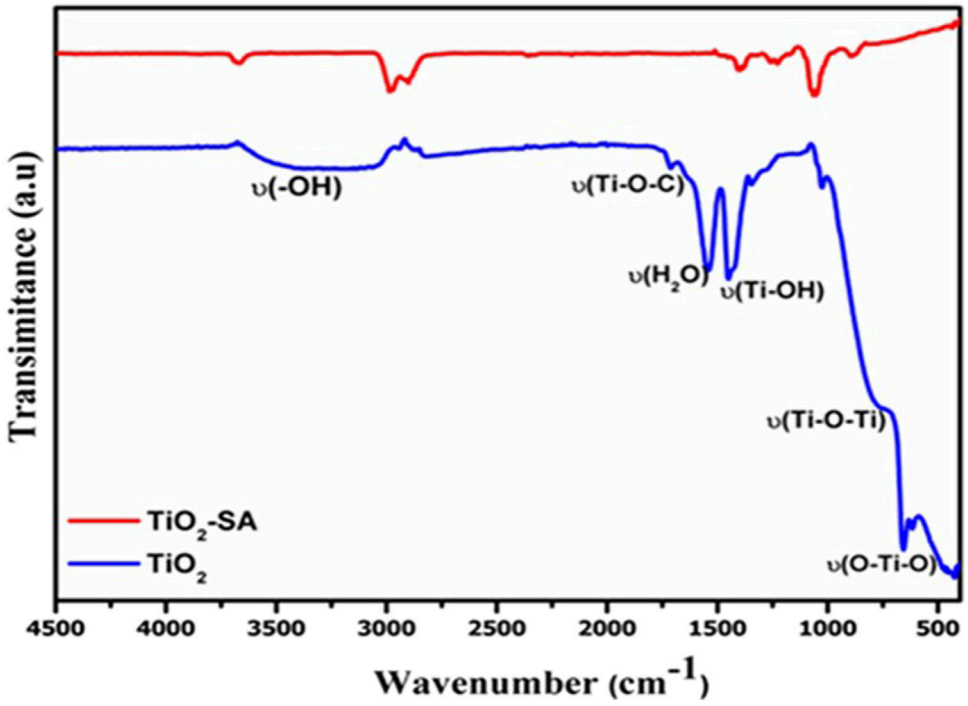

FIGURE 7
FTIR spectra for TiO_2 and TiO_2-sa.

metal oxide formation by sol-gel process, with the latter results aligning with FTIR (Figure 5A). Minor impurities are observed, such as Au and Pb, which are ascribed to gold-coating during sample preparation for SEM analysis. Small Pb (0.1 wt%) impurity may be attributed to contamination. It was observed that the surface morphology of TiO_2-sa improved agglomeration and reduced particle size upon the addition of a Triton X-100 surfactant. The results agreed strongly with TEM images (Figure 5). Huang et al., (2014) improved nickel particle dispersion by using various surfactants, including Triton X-100.

Figures 6A–F denote TiO_2-based materials which were investigated by HRTEM analysis. TiO_2 particles showed uneven morphology due to the coalescing of particles comprising big particles, single particles, and particle clusters forming larger aggregates. Average particle size was 65–85 nm. It was observed that the incorporation of Triton X-100 reduced the size of particles as chemical dispersant agents from 85 nm to 65 nm. Furthermore, the SAED pattern of the surfactant-assisted TiO_2 nano-powder exhibited a defined pattern, indicating a polycrystalline (polymorphic rings) nature Phattepur et al. (2019).

Figure 7 illustrates the FTIR spectra of TiO_2 –based materials. Typical metal oxide peaks were observed. The spectra showed the stretching vibrations of υ (O–Ti–O) around 580 cm^{-1} and ν(O–Ti–O) at 780 cm^{-1}, which indicated the characteristics of TiO_2 formation (Liu et al., 2012). Strong bending vibrations appearing at 1480.00 cm^{-1} and 1500.00 cm^{-1} were assigned to titanol υ (Ti–OH) and water molecules, respectively (Zhao et al., 2007). The consecutive peak around 1620 cm^{-1} was due to the asymmetric vibration of υ (C=O) bond and υ(Ti–O–C) bond from the used precursor, solvent, and hydrolyzing agent (Liu et al., 2012).

TABLE 3 Summary of elemental composition of TiO_2 from XRF.

Sample ID	Ti (%)	Conversion factor	TiO_2 (%)
TiO_2-1A	52.78	1.668	88.03
TiO_2-1B	52.73		87.96
Average	52.76		88.00
SD	0.03		0.05
RSD%	0.06		0.06
TiO_2-sa 2A	49.15	1.668	81.98
TiO_2-sa 2B	49.17		82.02
Average	49.16		82
SD	0.02		0.03
RSD %	0.04		0.04
CRM NIST 2711 3A	0.32	1.668	0.53
CRM NIST 3B	0.32		0.54
Actual value	0.306 ± 0.023		0.54 ± 0.023
Average	0.32		
SD	0.0		0.00
RSD %	0.00		0.00

The vibration around 2600 cm^{-1} was attributed to υ (=C–H) bond of solvent and surfactant (Liu et al., 2012; Ravishankar et al., 2020). The broad peak at 3300 cm^{-1} was ascribed to the hydroxyl (-OH) group

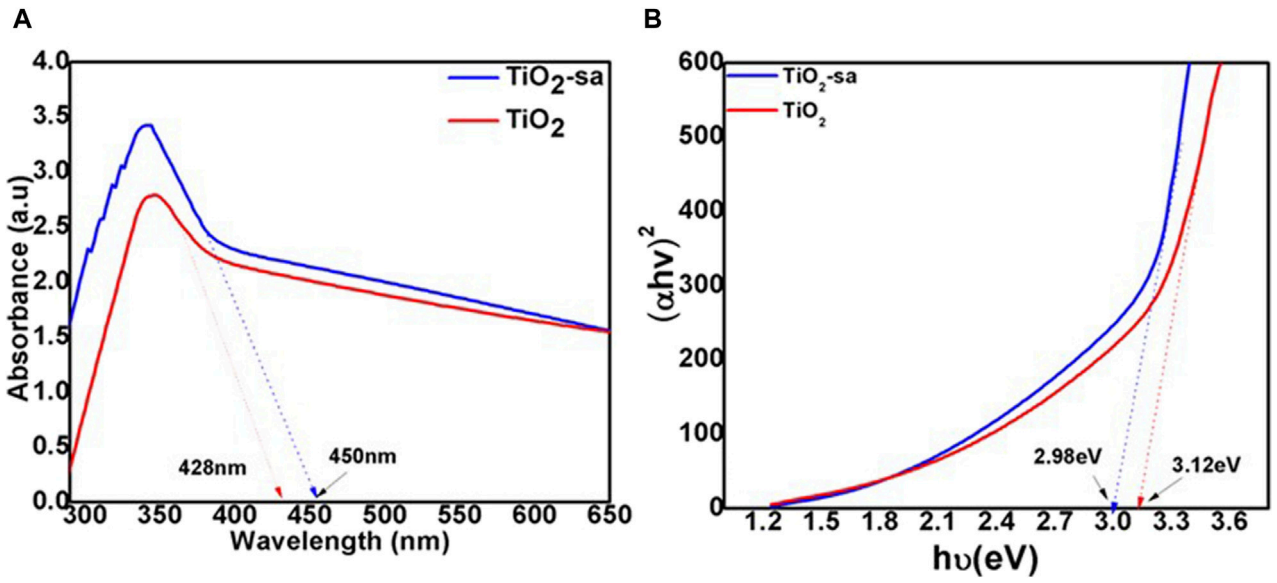

FIGURE 8
(A) UV-vis and **(B)** Tauc plot of TiO_2 and TiO_2-sa.

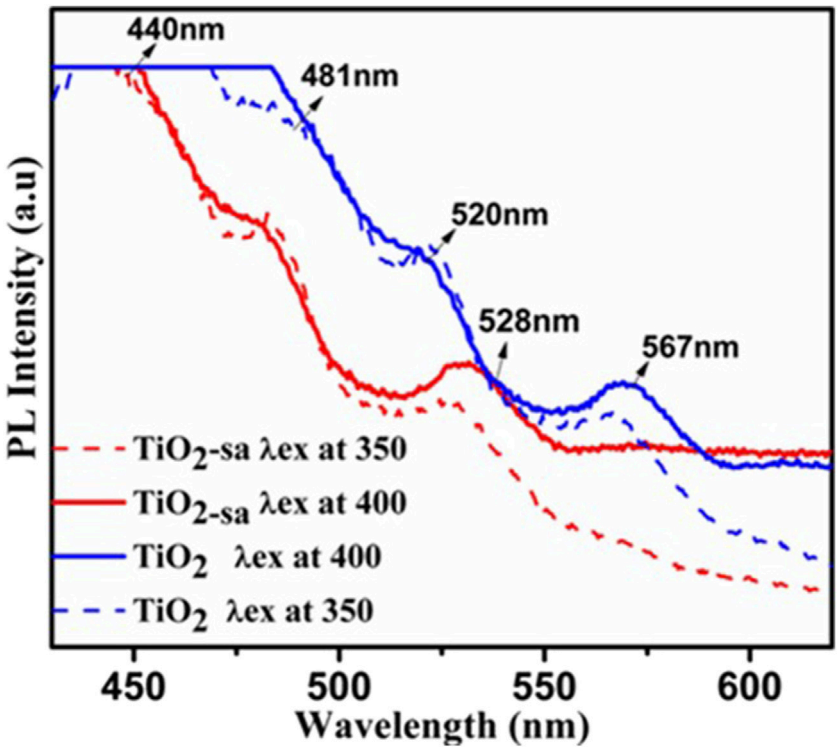

FIGURE 9
PL of TiO_2 and TiO_2-sa at 350 nm and 400 nm.

from adsorbed water molecules (Murashkevich et al., 2008; Sharma and Lee, 2020). It is noteworthy that the weak intensity for υ(Ti–O–Ti) reveal the lack of a rutile phase which aligned with XRD results (Figure 2). The υ(–OH) peak centering at around 3300 cm^{-1} was relatively weaker for TiO_2-sa, which might be due to the surface modification of TiO_2. In addition, the reduction in the intensity of (OH) vibration bands indicates the reduced amount of H_2O of crystallization in TiO_2-sa.

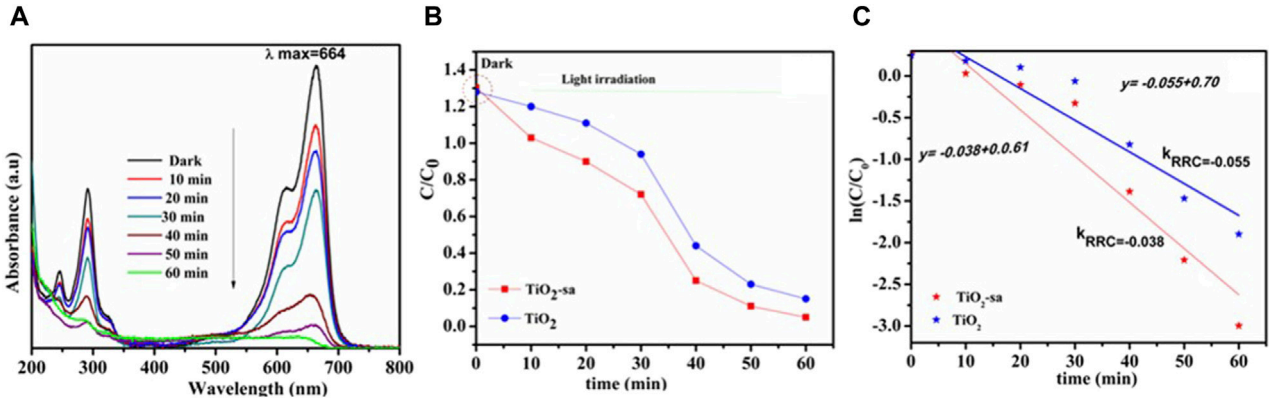

FIGURE 10
(A) Illustrated MB degradation of TiO_2 and **(B)** comparable MB degradation efficiency under visible light irradiation. **(C)** comparable degradation profile (rate constant).

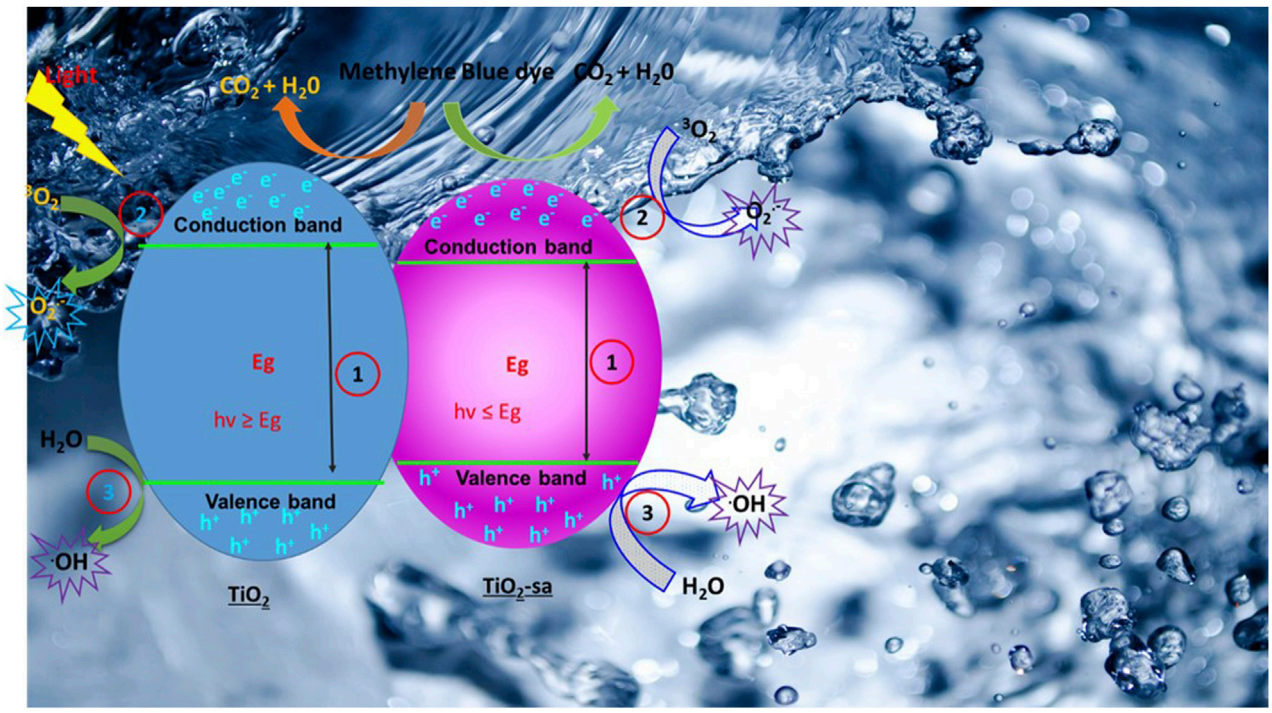

FIGURE 11
Mechanism of TiO_2-sa based photodegradation of MB.

4 Statistical analysis

All samples (TiO_2 and TiO_2-sa) including certified reference material (CRM) were run in duplicates, and the data was expressed into two decimals (Table 3). Using Horwitz to determine the closeness and differences of the values, the data indicated that both samples and CRMs were within acceptable limits. In addition, the elemental composition of TiO_2 is illustrated in Supplementary Figures S1, S2 and Table 3. It is evident that the composition of TiO_2 is 82%–88%. The results indicate the high purity of the as-synthesized TiO_2. The results for certified reference materials (CRM) —NIST 2711—exhibit 0.54%, which is within acceptable limits (0.54 ± 0.023) according to Horwitz, indicating the reproducibility, 99.99% recovery, and low relative standard deviation (RSD %). The later results show that the acceptable method developed using XRF Analyzer WingUI software is valid.

The UV-vis absorbance spectra of as-synthesized TiO_2 are illustrated in Figure 8A. TiO_2 and TiO_2-sa is dominated by the visible region around 475.00 and 500.00 nm, which is more redshifted than known TiO_2 absorption (380.00 nm). In addition, upon the addition of Triton X-100 on TiO_2 during sol-gel process, a significant bathochromic shift (higher wavelength from 475.00 to

500.00 nm) and enhanced absorbance were observed. Dubey (2018) reported a surfactant-free agglomerated TiO_2 synthesized sol-gel process; the wavelength obtained was <400 nm with the bandgap of 3.38 eV. Figure 7B confirms these results by displaying Tauc plot to estimate the optical bandgap as described Zhao et al. (2007). The band gap was reduced from 3.12 to 2.98 eV upon the incorporation of Triton X-100 as displayed in Figure 8B.

Figure 9 compares the photoluminescence (PL) of TiO_2 and TiO_2-sa controlled at the different excited wavelengths of 350 nm and 400 nm. It was established that the curves are similar in shape, suggesting that surfactant did not lead to a new PL phenomenon (Lellis et al., 2019; Murashkevich et al., 2008; Wang et al., 2018). However, TiO_2-sa exhibited blue-shift. The intense peak observed at around 440–480 nm is generally attributed to a hole–electron recombination [42]. At this wavelength, TiO_2-sa indicates the low intensity which may be ascribed to the reduction of the recombination reaction compared to the TiO_2 counterpart (Shindhal et al., 2021). The other peaks in a broad region from 481 to 561 nm originated from oxygen vacancies and Ti^{3+} (Zeng et al., 2019; Kasinathan et al., 2016), which is the transition of two electrons trapped in conduction to valance bands (band–band) (Dastan and Chaure, 2014). Generally, the increase in oxygen vacancies and surface defects corresponds to the increase in surface area (Wang et al., 2009; Chauhan et al., 2020). Moreover, this region (481–561) is attributed to the emission of bandgap transition and excitonic PL that resulted from the surface O_2 vacancies and surface defects. The PL of TiO_2-sa showed an enhanced surface defect induced by an enhanced surface area upon the addition of surfactant, suppressing the direct electron–photon (e^-/h^+) pair recombination (Li D. et al., 2020). These defects tend to create a new energy level just below the valence band which may create a trapping site and prevent recombination (Niu et al., 2020). This result indicates that TiO_2-sa exhibited higher surface area upon the addition of surfactant. It is believed that the surface area, crystallinity, and phase play a big role in the photocatalytic removal of organic pollutants such as MB, including textile dyes. Therefore, the PL results have a strong agreement with the photocatalytic results in Figure 10A.

Figures 10A and B denote the photodegradation curve of MB from 200 to 800 nm (Zhang et al., 2019; Hou et al., 2018; Wang et al., 2018). It was observed that absorbance and concentration decrease with time. The degradation efficiency (X) of the dye was calculated using Eq. 2

$$X(\%)\frac{A_0 - A_t}{A_0 - A_t} \times 100 \tag{2}$$

where X (%), A_0, and A_t represent the degradation efficiency, initial absorbance in zero irradiation, and absorbance after a given time interval, respectively. It can be seen that the dye photodegradation percentage increases with time until it reached 96.9% after an hour with TiO_2-sa (Figure 10A). Furthermore, TiO_2-sa showed an improvement in degradation as compared to its counterpart (TiO_2 = 75.36%) after 60 min of visible light irradiation. Due to this later result, it was believed that the photodegradation reaction rate followed the first-order Langmuir–Hinshelwood kinetics model. Therefore, the degradation rate was studied using Eq. 3:

$$\ln \frac{A_0}{A_t} = kt \tag{3}$$

where the degradation rate constant kt (k, min^{-1}) was determined from the slope of the straight line of $lin\frac{C_0}{C_t}$ against the time interval t (Figure 10C) as a function of the experimental parameters used. The value was 0.03 and 0.05 for TiO_2-sa and TiO^2 respectively.

The mechanism of activity of TiO_2 photocatalysts in MB degradation is depicted in Figure 11. In short, the TiO_2 photocatalysts produce holes in the valence band when they are exposed to UV light because of an electron transfer from the valence to conduction bands (**1**) (Mapukata and Nyokong, 2020; Sakar et al., 2019). The electrons and holes thus formed can readily reduce and oxidize the pollutants adsorbed on their surface. This is due to their ability to facilitate the formation of superoxide radicals (O^{2-}) from atmospheric oxygen (**2**) and hydroxyl radicals ($^{\cdot}OH$) from water (**3**). The photo-generated radicals can, in turn, oxidize and degrade organic materials like MB into CO_2 and H_2O (Kim et al., 2011; Madkhali et al., 2023).

5 Conclusion

A facile sol-gel was successfully applied to synthesize anatase TiO_2 nano-powders at low preparation and calcination temperatures. It was found that the addition of Triton X-100 modified the structure, morphology, and optical properties of TiO_2-based materials. Characterization of TiO_2 revealed that the use of Triton X-100 surfactants played a vital role by reducing the average crystalline size and triggering the polycrystalline phase. TEM images showed reduced particle size when surfactant was introduced. TGA confirmed that calcination at above 350 °C completely removed the surfactant, showed thermal stable TiO_2 based nano-powders. In addition, the incorporation of surfactant enhanced surface area and optical properties through UV-vis red-shift up to the visible region (510 nm) and optical bandgap reduction. The PL of TiO_2-sa showed enhanced oxygen vacancies induced by an enhanced surface area upon the addition of surfactant which inhibited the direct electron-photon (e/h^+) pair recombination. These results agree strongly with photocatalytic results. TiO_2-sa showed plausible structural and optical properties and higher photocatalytic dye degradation than its counterparts (pure TiO_2), making it a promising photocatalyst for the removal of organic pollutants in water.

Data availability statement

The original contributions presented in the study are included in the article/Supplementary Material; further inquiries can be directed to the corresponding author.

Author contributions

AM: Conceptualization, Formal Analysis, Methodology, Writing–original draft. T-CJ: Funding acquisition, Resources,

Supervision, Writing–review and editing. KL: Data curation, Writing–review and editing, SM: Data curation, Formal Analysis, Writing–review and editing. HM: Data curation, Software, Writing–review and editing. ML: Data curation, Formal Analysis, Writing–review and editing. NN: Data curation, Resources, Writing–review and editing. JT: Data curation, Funding acquisition, Resources, Supervision, Writing–review and editing.

Funding

The authors declare that financial support was received for the research, authorship, and/or publication of this article. This work was funded by Mintek grant number: ASR-00024035) and the University of Johannesburg.

Acknowledgments

The authors are grateful for the financial support from the Mintek and University of Johannesburg research council (URC).

Conflict of interest

The authors declare that the research was conducted in the absence of any commercial or financial relationships that could be construed as a potential conflict of interest.

Publisher's note

Supplementary material

The Supplementary Material for this article can be found online at: https://www.frontiersin.org/articles/10.3389/fceng.2024.1352283/full#supplementary-material

References

Allen, N. S., Mahdjoub, N., Vishnyakov, V., Kelly, P. J., and Kriek, R. J. (2018). The effect of crystalline phase (anatase, brookite and rutile) and size on the photocatalytic activity of calcined polymorphic titanium dioxide (TiO2). *Polym. Degrad. Stab.* 150, 31–36. doi:10.1016/j.polymdegradstab.2018.02.008

Alothman, Z. A. (2016). *A review: fundamental aspects of silicate mesoporous materials*. doi:10.3390/ma5122874

Anderson, C., and Bard, A. J. (1995). An improved photocatalyst of TiO2/SiO2 prepared by a sol-gel synthesis. *J. Phys. Chem.* 99 (24), 9882–9885. doi:10.1021/j100024a033

Andronic, L., Andrasi, D., Enesca, A., Visa, M., and Duta, A. (2011). The influence of titanium dioxide phase composition on dyes photocatalysis. *J. Sol-Gel Sci. Technol.* 58 (1), 201–208. doi:10.1007/s10971-010-2378-3

Attia, J. M. S. M., Wang, J., Wu, G., and Shen, J. (2002). Review on Sol-gel derived coatings: process, Techniques and optical application. *J.Mater. Sci. Technol.*

Andrade-Guel, M., Díaz-Jiménez, L., Cortés-Hernández, D., Cabello-Alvarado, C., Ávila-Orta, C., Bartolo-Pérez, P., et al. (2018). Microwave assisted sol – gel synthesis of titanium dioxide using hydrochloric and acetic acid as 8, pp. 171–177.

Bahar, M., Mozaffari, M., and Esmaeili, S. (2017). Effect of different alcohols, gelatinizing times, calcination and microwave on characteristics of TiO2 nanoparticles synthesized by sol–gel method. *J. Theor. Appl. Phys.* 11 (1), 79–86. doi:10.1007/s40094-017-0240-5

Basavarajappa, P. S., Patil, S. B., Ganganagappa, N., Reddy, K. R., Raghu, A. V., and Reddy, C. V. (2020). Recent progress in metal-doped TiO2, non-metal doped/codoped TiO2 and TiO2 nanostructured hybrids for enhanced photocatalysis. *Int. J. Hydrogen Energy* 45 (13), 7764–7778. doi:10.1016/j.ijhydene.2019.07.241

Casino, S., Di Lupo, F., Francia, C., Tuel, A., Bodoardo, S., and Gerbaldi, C. (2014). Surfactant-assisted sol gel preparation of high-surface area mesoporous TiO2 nanocrystalline Li-ion battery anodes. *J. Alloys Compd.* 594, 114–121. doi:10.1016/j.jallcom.2014.01.111

Chauhan, A., Verma, R., Kumari, S., Sharma, A., and Shandilya, P. (2020). *Photocatalytic dye degradation and antimicrobial activities of Pure and Ag-doped ZnO using Cannabis sativa leaf extract*, 1–16. doi:10.1038/s41598-020-64419-0

Dastan, D., and Chaure, N. B. (2014). Influence of surfactants on TiO2 nanoparticles grown by sol-gel technique. *Int. J. Mat. Mech. Manuf.* (January), 21–24. doi:10.7763/ijmmm.2014.v2.91

Dougna, A. A., Gombert, B., Kodom, T., Djaneye-Boundjou, G., Boukari, S. O., Leitner, N. K. V., et al. (2015). Photocatalytic removal of phenol using titanium dioxide deposited on different substrates: effect of inorganic oxidants. *J. Photochem. Photobiol. A Chem.* 305, 67–77. doi:10.1016/j.jphotochem.2015.02.012

Dubey, R. S. (2018). Temperature-dependent phase transformation of TiO2 nanoparticles synthesized by sol-gel method. *Mat. Lett.* 215, 312–317. doi:10.1016/j.matlet.2017.12.120

Fang, R., Liang, Y., Ge, X., Du, M., Li, S., Li, T., et al. (2015). Preparation and photocatalytic degradation activity of TiO2/rGO/polymer composites. *Colloid Polym. Sci.* 293 (4), 1151–1157. doi:10.1007/s00396-015-3507-x

Feinle, A., Heugenhauser, A., and Hüsing, N. (2015). Impact of surfactants and acids on the sol-gel synthesis of MgO aerogels. *J. Supercrit. Fluids* 106, 133–139. doi:10.1016/j.supflu.2015.06.019

Galkina, O. L., Vinogradov, V. V., Agafonov, A. V., and Vinogradov, A. V. (2011). Surfactant-assisted sol-gel synthesis of TiO 2 with uniform particle size distribution. *Int. J. Inorg. Chem.* 2011, 1–8. doi:10.1155/2011/108087

Hanaor, D. A. H., and Sorrell, C. C. (2011). Review of the anatase to rutile phase transformation. *J. Mat. Sci.* 46 (4), 855–874. doi:10.1007/s10853-010-5113-0

Hou, C., Hu, B., and Zhu, J. (2018). Photocatalytic degradation of methylene blue over TiO2 pretreated with varying concentrations of NaOH. *Catalysts* 8 (12), 575–613. doi:10.3390/catal8120575

Huang, G. Y., Xu, S. M., Li, L. Y., and Wang, X. J. (2014). Effect of surfactants on dispersion property and morphology of nano-sized nickel powders. *Trans. Nonferrous Met. Soc. China Engl. Ed.* 24 (11), 3739–3746. doi:10.1016/S1003-6326(14)63523-8

Id, O., "Properties and microstructural aspects of TiO 2 doped sintered Alumina-Zirconia composite ceramics," *J. Appl. Ceram. Technol.*, pp. 0–3. 2018. doi:10.1111/ijac.13021

Karami, A. (2010). Synthesis of TiO2 nano powder by the sol-gel method and its use as a photocatalyst. *J. Iran. Chem. Soc.* 7 (2), 154–160. doi:10.1007/bf03246194

Kasinathan, K., Kennedy, J., Elayaperumal, M., Henini, M., and Malik, M. (2016). Photodegradation of organic pollutants RhB dye using UV simulated sunlight on ceria based TiO2 nanomaterials for antibacterial applications. *Sci. Rep.* 6 (November), 38064–38112. doi:10.1038/srep38064

Kim, S. J., Seo, S. G., Lee, D. J., Lee, H., Park, S. H., et al. (2011). Photocatalyzed destruction of organic dyes using microwave/UV/O 3/H2O2/TiO2 oxidation system. *Catal. Today* 164 (1), 384–390. doi:10.1016/j.cattod.2010.10.025

Kubiak, A., Bielan, Z., Bartkowiak, A., Gabała, E., Piasecki, A., Zalas, M., et al. (2020). Synthesis of titanium dioxide via surfactantassisted microwave method for photocatalytic and dye-sensitized solar cells applications. *Catalysts* 10 (5), 586. doi:10.3390/catal10050586

Lellis, B., Fávaro-Polonio, C. Z., Pamphile, J. A., and Polonio, J. C. (2019). Effects of textile dyes on health and the environment and bioremediation potential of living organisms. *Biotechnol. Res. Innov.* 3 (2), 275–290. doi:10.1016/j.biori.2019.09.001

Li, D., Song, H., Meng, X., Shen, T., Sun, J., Han, W., et al. (2020b). Effects of particle size on the structure and photocatalytic performance by alkali-treated TiO2. *Nanomaterials* 10 (3), 546–614. doi:10.3390/nano10030546

Li, J., Zeng, Y., Fang, Y., Chen, N., Du, G., and Zhang, A. (2020a). Synthesis of (La + Nb) co-doped TiO 2 rutile nanoparticles and dielectric properties of their derived ceramics composed of submicron-sized grains. *Ceram. Int.* 47 (December), 8859–8867. doi:10.1016/j.ceramint.2020.12.007

Liang, Y., Sun, S., Deng, T., Ding, H., Chen, W., and Chen, Y. (2018). The preparation of TiO2 film by the sol-gel method and evaluation of its self-cleaning property. *Mater. (Basel)* 11 (3), 450–512. doi:10.3390/ma11030450

Liu, Z., Jian, Z., Fang, J., Xu, X., Zhu, X., and Wu, S. (2012). Low-temperature reverse microemulsion synthesis, characterization, and photocatalytic performance of nanocrystalline titanium dioxide. *Int. J. Photoenergy* 2012 (February), 1–8. doi:10.1155/2012/702503

Madkhali, N., Prasad, C., Malkappa, K., Choi, H. Y., Govinda, V., Bahadur, I., et al. (2023). Recent update on photocatalytic degradation of pollutants in waste water using TiO2-based heterostructured materials. *Results Eng.* 17 (January), 100920. doi:10.1016/j.rineng.2023.100920

Mahshid, S., Askari, M., and Ghamsari, M. S. (2007). Synthesis of TiO2 nanoparticles by hydrolysis and peptization of titanium isopropoxide solution. *J. Mat. Process. Technol.* 189 (1–3), 296–300. doi:10.1016/j.jmatprotec.2007.01.040

Mapukata, S., and Nyokong, T. (2020). Development of phthalocyanine functionalised TiO2and ZnO nanofibers for photodegradation of methyl orange. *New J. Chem.* 44 (38), 16340–16350. doi:10.1039/d0nj03326j

Mohamad Saad, P. S., Sutan, H. B., Shariffudin, S. S., Hashim, H., and Mohd Noor, U. (2015). TiO2 thin film via sol-gel method: investigation on molarity effect. *IOP Conf. Ser. Mat. Sci. Eng.* 99 (1), 012006. doi:10.1088/1757-899X/99/1/012006

Murashkevich, A. N., Lavitskaya, A. S., Barannikova, T. I., and Zharskii, I. M. (2008). Infrared absorption spectra and structure of TiO2-SiO 2 composites. *J. Appl. Spectrosc.* 75 (5), 730–734. doi:10.1007/s10812-008-9097-3

Niu, P., Wu, G., Chen, P., Zheng, H., Cao, Q., and Jiang, H. (2020). Optimization of boron doped TiO2 as an efficient visible light-driven photocatalyst for organic dye degradation with high reusability. *Front. Chem.* 8 (March), 172–178. doi:10.3389/fchem.2020.00172

Ola, O., and Maroto-Valer, M. M. (2015). Review of material design and reactor engineering on TiO2 photocatalysis for CO2 reduction. *J. Photochem. Photobiol. C Photochem. Rev.* 24, 16–42. doi:10.1016/j.jphotochemrev.2015.06.001

Phattepur, H., Siddaiah, G. B., and Ganganagappa, N. (2019). Synthesis and characterisation of mesoporous TiO2 nanoparticles by novel surfactant assisted sol-gel method for the degradation of organic compounds. *Period. Polytech. Chem. Eng.* 63 (1), 85–95. doi:10.3311/PPch.11789

Ravishankar, T. N., Vaz, M. D. O., and Teixeira, S. R. (2020). The effects of surfactant in the sol-gel synthesis of CuO/TiO2 nanocomposites on its photocatalytic activities under UV-visible and visible light illuminations. *New J. Chem.* 44 (5), 1888–1904. doi:10.1039/c9nj05246a

Sakar, M., Mithun Prakash, R., and Trong-On, D. (2019). Insights into the tio2-based photocatalytic systems and their mechanisms. *Catalysts* 9 (8), 680. doi:10.3390/catal9080680

Sharma, A. K., and Lee, B. K. (2020). Surfactant-aided sol-gel synthesis of TiO2–MgO nanocomposite and their photocatalytic azo dye degradation activity. *J. Compos. Mat.* 54 (12), 1561–1570. doi:10.1177/0021998316636464

Shindhal, T., Rakholiya, P., Varjani, S., Pandey, A., Ngo, H. H., Guo, W., et al. (2021). A critical review on advances in the practices and perspectives for the treatment of dye industry wastewater. *Bioengineered* 12 (1), 70–87. doi:10.1080/21655979.2020.1863034

Tahir, M., and Amin, N. A. S. (2015). Indium-doped TiO2 nanoparticles for photocatalytic CO2 reduction with H2O vapors to CH4. *Appl. Catal. B Environ.* 162, 98–109. doi:10.1016/j.apcatb.2014.06.037

Thiruvengadathan, R., Korampally, V., Ghosh, A., Chanda, N., Gangopadhyay, K., and Gangopadhyay, S. (2013). Nanomaterial processing using self-assembly-bottom-up chemical and biological approaches. *Rep. Prog. Phys.* 76 (6), 066501. doi:10.1088/0034-4885/76/6/066501

Wang, E., Yang, W., and Cao, Y. (2009). Unique surface chemical species on indium doped TiO2 and their effect on the visible light photocatalytic activity. *J. Phys. Chem. C* 113 (49), 20912–20917. doi:10.1021/jp9041793

Wang, X. Q., Han, S. F., Zhang, Q. W., Zhang, N., and Zhao, D. D. (2018). Photocatalytic oxidation degradation mechanism study of methylene blue dye waste water with GR/iTO 2. *MATEC Web Conf.* 238, 03006. doi:10.1051/matecconf/201823803006

Wang, Y., Li, L., Huang, X., Li, Q., and Li, G. (2015). New insights into fluorinated TiO2 (brookite, anatase and rutile) nanoparticles as efficient photocatalytic redox catalysts. *RSC Adv.* 5 (43), 34302–34313. doi:10.1039/c4ra17076h

Wetchakun, N., and Phanichphant, S. (2008). Effect of temperature on the degree of anatase-rutile transformation in titanium dioxide nanoparticles synthesized by the modified sol-gel method. *Curr. Appl. Phys.* 8 (3–4), 343–346. doi:10.1016/j.cap.2007.10.028

Wong, A., Daoud, W. A., Liang, H., and Szeto, Y. S. (2014). The effect of aging and precursor concentration on room-temperature synthesis of nanocrystalline anatase TiO2. *Mat. Lett.* 117, 82–85. doi:10.1016/j.matlet.2013.11.056

Wu, H. H., Yu, Y., Zhu, B. L., Wang, S. R., Huang, W. P., Wu, S. H., et al. (2008). Preparation and characterization of bismuth doped TiO2 thin films. *J. Dispers. Sci. Technol.* 29 (10), 1471–1475. doi:10.1080/01932690802313642

You, Y. F., Xu, C., Xu, S., Cao, S., Wang, J., Huang, Y., et al. "Structural characterization and optical property of TiO 2 powders prepared by the sol – gel method," *Ceram. Int.* vol. 40, pp. 8659–8666. 2014. doi:10.1016/j.ceramint.2014.01.083

Zeng, G., Zhang, Q., Liu, Y., Zhang, S., and Guo, J. (2019). Preparation of TiO2 and fe-TiO2 with an impinging stream-rotating packed bed by the precipitation method for the photodegradation of gaseous toluene. *Nanomaterials* 9 (8), 1173–1217. doi:10.3390/nano9081173

Zhai, Y. Q., Jing, Q., and Zhang, Z. (1990). The sol-gel process. *Chem. Rev.* 90, 33–72. doi:10.1021/cr00099a003

Zhang, X., Xiao, J., Peng, C., Xiang, Y., and Chen, H. (2019). Enhanced photocatalytic hydrogen production over conjugated polymer/black TiO 2 hybrid: the impact of constructing active defect states. *Appl. Surf. Sci.* 465, 288–296. doi:10.1016/j.apsusc.2018.09.105

Zhao, Y., Liu, X., Gu, F., Jiang, H., Shao, W., et al. (2007). Synthesis and optical properties of TiO2 nanoparticles. *Mat. Lett.* 61 (1), 79–83. doi:10.1016/j.matlet.2006.04.010

Zhou, Y. (2020). Controllable design, synthesis and characterization of nanostructured rare earth metal oxides. *Phys. Sci. Rev.* 5 (3), 1–49. doi:10.1515/psr-2018-0084